

Predictability of the Madden–Julian Oscillation Estimated Using Observational Data

RUIQIANG DING AND JIANPING LI

State Key Laboratory of Numerical Modeling for Atmospheric Sciences and Geophysical Fluid Dynamics (LASG), Institute of Atmospheric Physics, Chinese Academy of Sciences, Beijing, China

KYONG-HWAN SEO

Division of Earth Environmental System, Department of Atmospheric Sciences, Pusan National University, Busan, South Korea

(Manuscript received 2 June 2009, in final form 16 September 2009)

ABSTRACT

Existing numerical models produce large error in simulating the Madden–Julian oscillation (MJO), thereby underestimating its predictability. In this paper, the predictability limit of the MJO is determined by the nonlinear local Lyapunov exponent approach, which provides an estimate of atmospheric predictability based on the observational data. The results show that the predictability limit of the MJO obtained from the bandpass-filtered (30–80 days) outgoing longwave radiation and wind fields, which serves as an empirical estimate of the theoretical potential predictability of the MJO, can exceed 5 weeks, which is well above the 1-week predictability of background noise caused by bandpass filtering. In contrast, a real-time analysis of MJO predictability using the real-time multivariate MJO (RMM) index, as introduced by Wheeler and Hendon, reveals a predictability limit of about 3 weeks. The findings reported here raise the possibility of obtaining a higher predictability limit in real-time prediction by improving the RMM index or by introducing a better method of extracting intraseasonal signals.

1. Introduction

The Madden–Julian Oscillation (MJO), one of the dominant modes of low-frequency variability in the tropical troposphere (Wang and Rui 1990; Madden and Julian 1994), is characterized by an eastward progression of large regions of both enhanced and suppressed tropical rainfall, observed mainly over the Indian Ocean and the western Pacific Ocean. The MJO affects a wide range of tropical weather and climate, including tropical cyclone formation (Nakazawa 1986; Hartmann et al. 1992; Liebmann et al. 1994) and the onset and breaks of the Asian–Australian monsoon system (Yasunari 1980; Lau and Chan 1986). Furthermore, previous studies have shown that the MJO influences the variability and predictability of extratropical circulation (Ferranti et al. 1990; Higgins and Mo 1997; Jones et al. 2004). Hence,

the ability to make extended-range predictions of the MJO could have global impacts.

Given the importance of the MJO in its interactions with the tropical and extratropical circulation anomalies, it is of great interest to investigate its upper limit of predictability. For example, information on the MJO predictability limit could be used as a basic guideline for the future improvement of forecast models. However, the limit of the predictability of the MJO phenomenon remains an open issue. A number of recent studies have demonstrated that the useful skill of the MJO in existing numerical and statistical models can reach about 15–20 days (e.g., Goswami and Xavier 2003; Fu et al. 2007; Jiang et al. 2008; Seo et al. 2009). Considering the intuitive notion that predictability for a given process should be approximately proportional to its lifetime (Van den Dool and Saha 1990), long-range predictability (from 4 weeks to 2 months) of the MJO has been often hypothesized. By comparison, the predictability range for the MJO of 15–20 days is short relative to the leading time scales of the MJO, and existing models very

Corresponding author address: Jianping Li, Bei-chen-xi-lu, Chaoyang District, No. 40 Building, Beijing 100029, China.
E-mail: ljp@lasg.iap.ac.cn

likely underestimate the predictability of the MJO. The main reason for this limited predictability range is considered to be the deficiencies in existing models. Almost all statistical forecast models and dynamical models show poor performances in simulating the MJO (Waliser et al. 2003; Seo et al. 2005, 2007); they consequently fail to provide an adequate measure of the upper limit of MJO predictability. Reichler and Roads (2005) demonstrated that when the model and the initial and boundary conditions are all perfect the useful forecast skill of the MJO is about 4 weeks. In addition, Waliser et al. (2003) reported a theoretically possible MJO forecast limit extending out to ~ 30 days for 200-hPa velocity potential. These results indicate that further improvements in the prediction skill of the MJO may be obtainable through enhancements to existing models.

The objective of this study is to determine the predictability limit of the MJO based on the observational data. The observational data contain almost all of the real information regarding the structure and propagation characteristics of the MJO, including its variability, intensity, and large-scale eastward propagation. Given the lack of realistic models in predicting the MJO, it is more appropriate to determine its predictability limit based on the observational data. Recently, a new approach using the nonlinear local Lyapunov exponent (NLLE) was introduced to investigate atmospheric predictability (Li et al. 2006; Ding and Li 2007). With the NLLE and its derivatives, the limit of dynamical predictability of chaotic systems can be quantitatively determined. To apply the NLLE approach to the study of actual atmospheric predictability, a reasonable and efficient algorithm has been devised to enable the estimation of the NLLE and its derivatives based on the observational data (Ding et al. 2008). In accord with this, the predictability of the MJO can be assessed using the NLLE method. We note that the predictability of the MJO obtained by using the observational data would be close to the upper limit of MJO predictability. The predictability limit of the MJO, as estimated according to this approach, may only be attained when the models are able to realistically simulate the MJO with small initial errors.

2. Application of the NLLE approach

For systems whose equations of motion are explicitly known, such as the Lorenz system, we can directly calculate the mean NLLE by the numerical integration of the Lorenz system and its error evolution equations (Ding and Li 2007). However, the dynamic equations of atmospheric motion are explicitly unknown, and we are unable to accurately estimate the dimensions of the

atmosphere system. Large amounts of atmospheric observational data are available. In fact, we may estimate the NLLE by making use of large amounts of such data. In a previous study, we developed an algorithm that yields estimates of the NLLE and its derivatives based on atmospheric observational data (Ding et al. 2008). The general idea of the algorithm is to find local analogs of evolution pattern from observational time series. The local analog is based on the evolution information at two different time points in the time series. If the evolutions of two different time points are analogous over a very short interval, it is very likely that the two points were analogous at the initial time. This analog is referred to as a "local dynamical analog." The NLLE is estimated by calculating the mean exponential divergence rate of initially analogous points. The predictability can be quantitatively determined by investigating the average growth of initial errors, which is derived from the NLLE. The initial errors in the NLLE calculation are determined by the average distance between initially analogous points. Given a sufficient period of observation data, the average distance between initially analogous points is relatively small; the initial errors in the NLLE calculation are also small. If we gradually change the length of the period of observation data, the initial errors also slowly vary accordingly. The resultant predictability is found to be insensitive to the changes in initial errors.

Two examples (the Lorenz system and the Henon map) reveal that the algorithm is completely applicable in terms of estimating the mean error growth from an experimental time series. The algorithm can also be applied to the study of atmospheric predictability. Based on observational data, the NLLE approach has been used to investigate decadal changes in weather predictability (Ding et al. 2008) and the temporal-spatial distributions of the predictability of monthly and seasonal means of climate variables (Li and Ding 2008). Our results show that the predictability limit of daily geopotential height and wind fields in the troposphere is about 2 weeks, consistent with previous studies (Lorenz 1965, 1982). In this study, we explore the predictability limit of the MJO based on the NLLE approach.

3. Data

Outgoing longwave radiation (OLR) data are used as a proxy for tropical convective activity, whereby low values of OLR indicate the presence of tall cumulus towers associated with intense convection (Waliser et al. 1993). The OLR data are daily averaged values from the National Oceanic and Atmospheric Administration polar-orbiting series of satellites (Liebmann and Smith

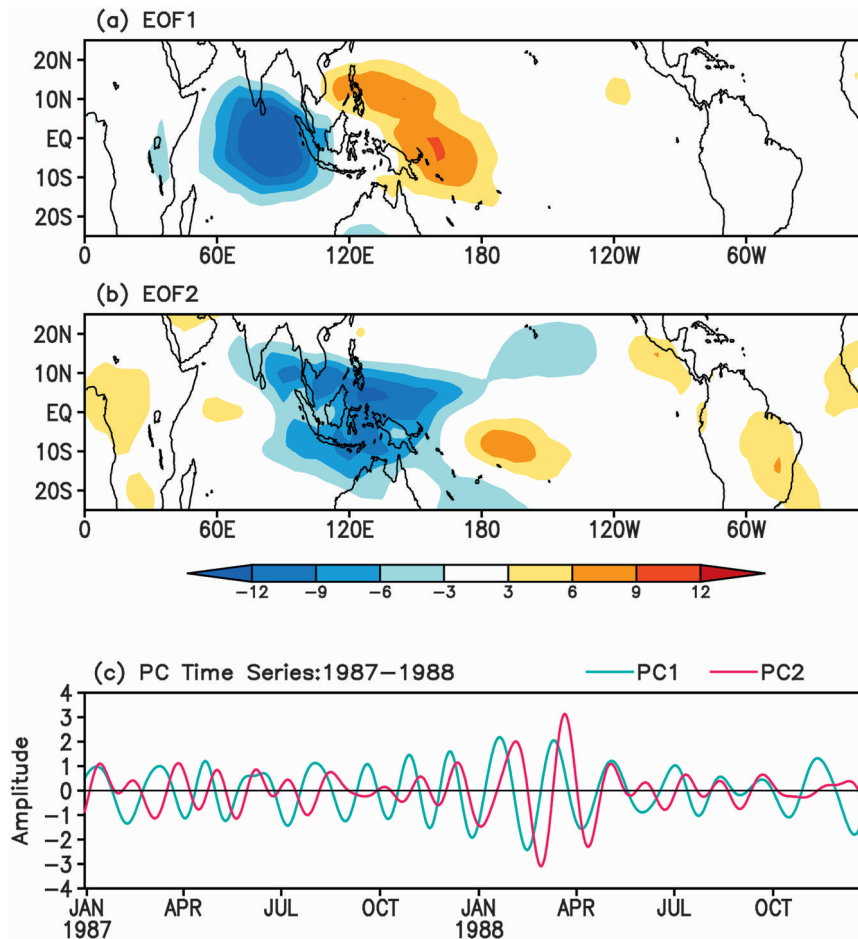


FIG. 1. EOF analysis of 30–80-days-filtered OLR over the tropics (25°S – 25°N): (a) EOF1, (b) EOF2, and (c) PC1 and PC2 from 1 Jan 1987 to 31 Dec 1988.

1996). The data are continuous in time from 1 June 1974 to 16 March 1978 and from 1 January 1979 to the present, with data missing from 17 March 1978 to 31 December 1978. Here we use the continuous 1979–2008 time series in the global tropical strip (25°S – 25°N). To add some confidence to the predictability limit obtained from OLR data, a similar record of 850- and 200-hPa zonal winds from the National Centers for Environmental Prediction–National Center for Atmospheric Research reanalysis (Kalnay et al. 1996) is also employed. Both the OLR and zonal winds are analyzed on a 2.5° latitude–longitude grid.

4. Results

To isolate the MJO signal of the OLR, the time mean and first three harmonics of the annual cycle are removed from the OLR time series, which are then passed through a 30–80-days bandpass Lanczos filter. Empirical orthogonal function (EOF) analysis is performed on the

filtered OLR over the tropics from 25°S to 25°N , following Matthews (2000). The spatial structures of the leading two EOFs of the filtered OLR are presented in Fig. 1. EOF1 and EOF2 account for 9.0% and 7.3% of the variance, respectively, and are well separated from the remaining EOFs, based on the criteria of North et al. (1982) (EOF3 explains only 3.7% of the variance). EOF1 describes the familiar MJO convective dipole, with negative OLR anomalies (enhanced convection) over the Indian Ocean and positive OLR anomalies (reduced convection) over the western Pacific (Fig. 1a). EOF2 has enhanced convection over the “Maritime Continent,” reduced convection over the South Pacific convergence zone, South America, and Africa (Fig. 1b), and is spatially in quadrature with EOF1. Taken as a pair, these structures are similar to the EOFs of the MJO obtained by Matthews (2000). The principal component (PC) time series show the time-varying amplitude of the EOF spatial structures. A 2-yr subset of the PC time series (1987–88) is shown in Fig. 1c. PC1

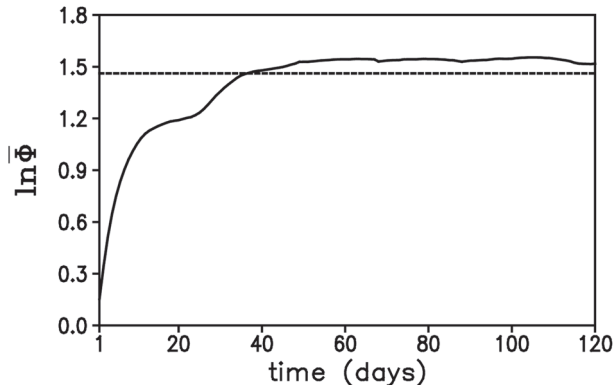


FIG. 2. Mean error growth of the vector \mathbf{Z} in the two-dimensional phase space defined by the first two PCs of EOF analysis of filtered OLR data. The dashed line represents the 95% level of saturation value, as obtained by taking the average of the mean error growth after 80 days.

leads PC2 by about one-quarter of a cycle, consistent with the eastward propagation of the MJO.

The MJO can be represented by the vector \mathbf{Z} in the two-dimensional phase space defined by the first two PCs:

$$\mathbf{Z}(t) = [\text{PC1}(t), \text{PC2}(t)]. \quad (1)$$

The error of \mathbf{Z} is measured as the absolute error $[(\Delta\text{PC1})^2 + (\Delta\text{PC2})^2]^{1/2}$, where ΔPC1 represents the error in the PC1 axis and ΔPC2 represents the error in the PC2 axis. In the two-dimensional phase space, the mean error growth of \mathbf{Z} with time can be obtained using the NLE approach. Figure 2 shows that the mean error of \mathbf{Z} initially increases quickly, then slows down, and finally reaches saturation. Once the error growth reaches the saturation level, almost all information on initial states is lost and the prediction becomes meaningless. Using the saturation level, the limit of dynamic predictability can be quantitatively determined. To reduce the effects of sampling fluctuations, the predictability limit is defined as the time at which the error reaches 95% of its saturation level. From Fig. 2, the predictability limit of OLR data temporally filtered for the MJO is about 36 days.

Ding and Li (2007) proposed a theorem that states that for chaotic systems the error growth will eventually reach saturation. In the case presented here, the error of the MJO reaches saturation, suggesting that the nature of the MJO is chaotic and is essentially difficult to predict. Figure 2 also reveals that the mean error of \mathbf{Z} shows a quick increase in the initial 2 weeks, after which it shows a slow increase until the saturation (this pattern is also evident in Figs. 4 and 6, described below), possibly indicating that the initial conditions play an important role in determining the initial error growth of the MJO;

after about 2 weeks, the error growth is more strongly influenced by the slow-varying boundary conditions. This result is consistent with the previous studies, which found that the external forcing offered by intraseasonal SST anomalies can extend the MJO predictability to a long lead time (Reichler and Roads 2005; Fu et al. 2007; Kim et al. 2008).

To investigate the predictability limit of the dynamic variables associated with the MJO, we used the 850-hPa zonal wind anomalies averaged from 5°S to 5°N. EOF analysis was performed on the resulting equatorially averaged zonal wind for the entire record (1979–2008) after applying a 30–80-days Lanczos filter. Figure 3a shows the EOF1 and EOF2 of the filtered 850-hPa zonal wind. EOF1 and EOF2 explain 32.9% and 21.9% of the variance, respectively, while EOF3 explains 8.6%. Using the criterion of North et al. (1982), the first two EOFs are significantly different from the rest. EOF1 and EOF2 appear to form a propagating signal in the zonal wind. EOF1 shows low-level westerly wind anomalies over the Indian Ocean that switch to low-level easterlies over the Pacific at roughly 130°E. EOF2 is spatially in quadrature with EOF1, with low-level westerly wind anomalies over the western and central Pacific. The spatial structures of EOF1 and EOF2 are generally consistent with those presented in Maloney and Hartmann (1998). Figure 3b shows the PC time series of 850-hPa zonal wind for 1987–88. Similar to Fig. 1c, a period of strong MJO events appears from 1 December 1987 to 1 April 1988, and PC1 leads PC2 by approximately one-quarter of a cycle. As in Eq. (1), \mathbf{Z} , consisting of PC1 and PC2, represents the MJO activity. The mean error of \mathbf{Z} is shown in Fig. 4, as calculated using the NLE approach. According to the criterion of 95% saturation error, the predictability limit of the MJO is determined to be approximately 39 days. This predictability, determined from 850-hPa zonal wind, is comparable to (but slightly higher than) that determined from the OLR. However, previous studies suggest that the predictability of some dynamic fields associated with the MJO in numerical models is much longer than that of MJO-related rainfall (Waliser et al. 2003; Reichler and Roads 2005). The relatively low predictability of rainfall is probably due to relatively large deficiencies of the models (with forecast errors tending to grow rapidly) in simulating the convective rainfall. The application of observational data in this paper excludes the influences of model deficiencies, meaning that the similar predictabilities of 850-hPa zonal wind and OLR can be obtained.

Figures 1 and 3 show the EOFs of a single tropically confined field that has been bandpass filtered to intraseasonal periods. To capture the convective and

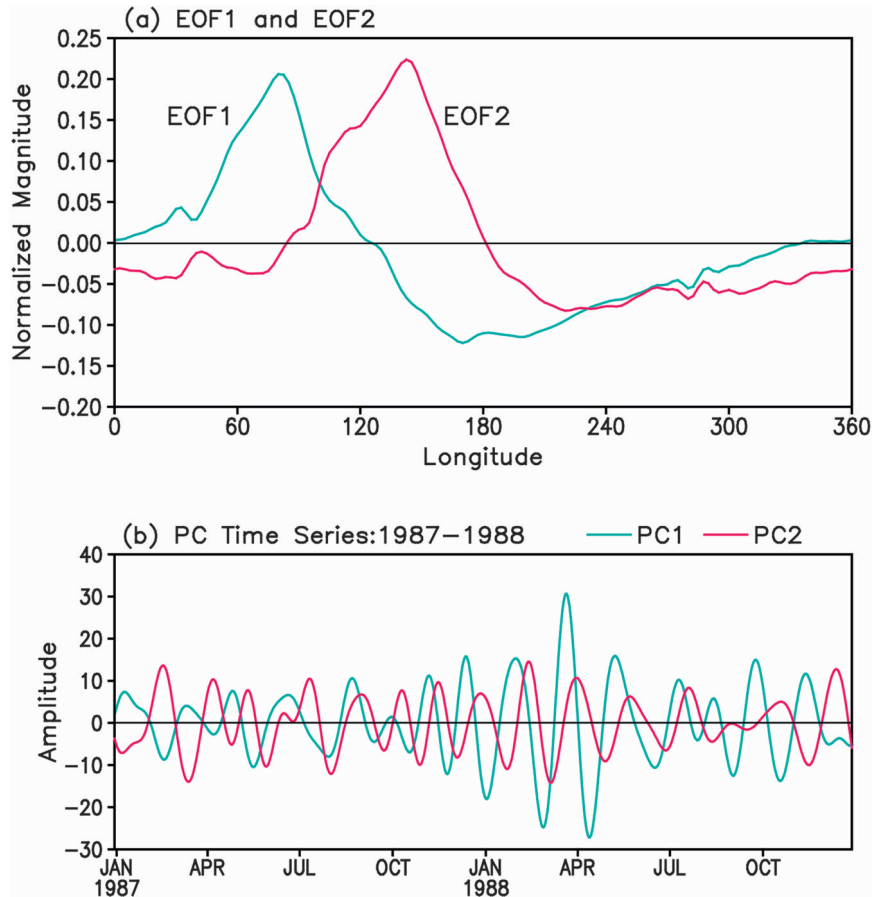


FIG. 3. EOF analysis of near-equatorially averaged (5°S – 5°N) 850-hPa zonal wind: (a) EOF1 and EOF2 and (b) PC1 and PC2 from 1 Jan 1987 to 31 Dec 1988.

baroclinic zonal wind structure of the MJO, we perform an EOF analysis of the combined fields of near-equatorially averaged (5°S – 5°N) OLR and 850- and 200-hPa zonal winds. Before the EOF analysis, the annual cycles of the near-equatorially averaged fields were removed and intraseasonal periods were captured using a 30–80-days Lanczos filter. In computing EOFs of combined fields, each field was normalized by its global variance (longitudinally averaged variance) before input, following the method of Wheeler and Hendon (2004) and Seo et al. (2009). Figure 5 shows the spatial structures of the leading two EOFs of the combined fields. EOF1 and EOF2 account for 22.1% and 20.9% of the variance, respectively, and are well separated from the remaining EOFs (EOF3 explains only 5.5% of the variance). EOF1 describes the familiar situation in which enhanced convection (negative OLR anomalies) exists at the longitudes of the western Pacific: low-level westerly wind anomalies occur near and to the west of the convection, and low-level easterly wind anomalies occur to the east of the enhanced convection; upper-

level wind anomalies are in the opposite direction of those at lower levels (Fig. 5a). EOF2 has enhanced convection over the eastern Indian Ocean and Maritime Continent associated with wind patterns that are in close

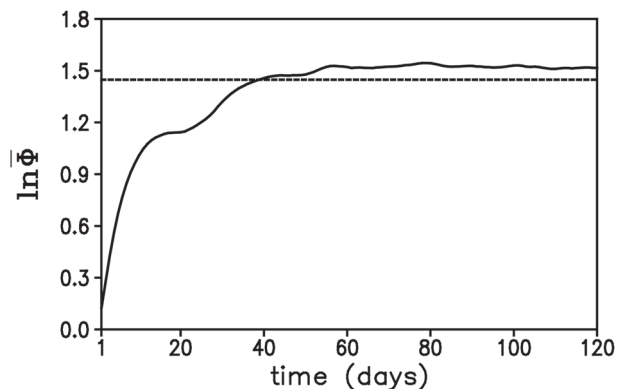


FIG. 4. As in Fig. 2, but for mean error growth of \mathbf{Z} in the two-dimensional phase space defined by the first two PCs of EOF analysis of filtered 850-hPa zonal wind (see Fig. 3).

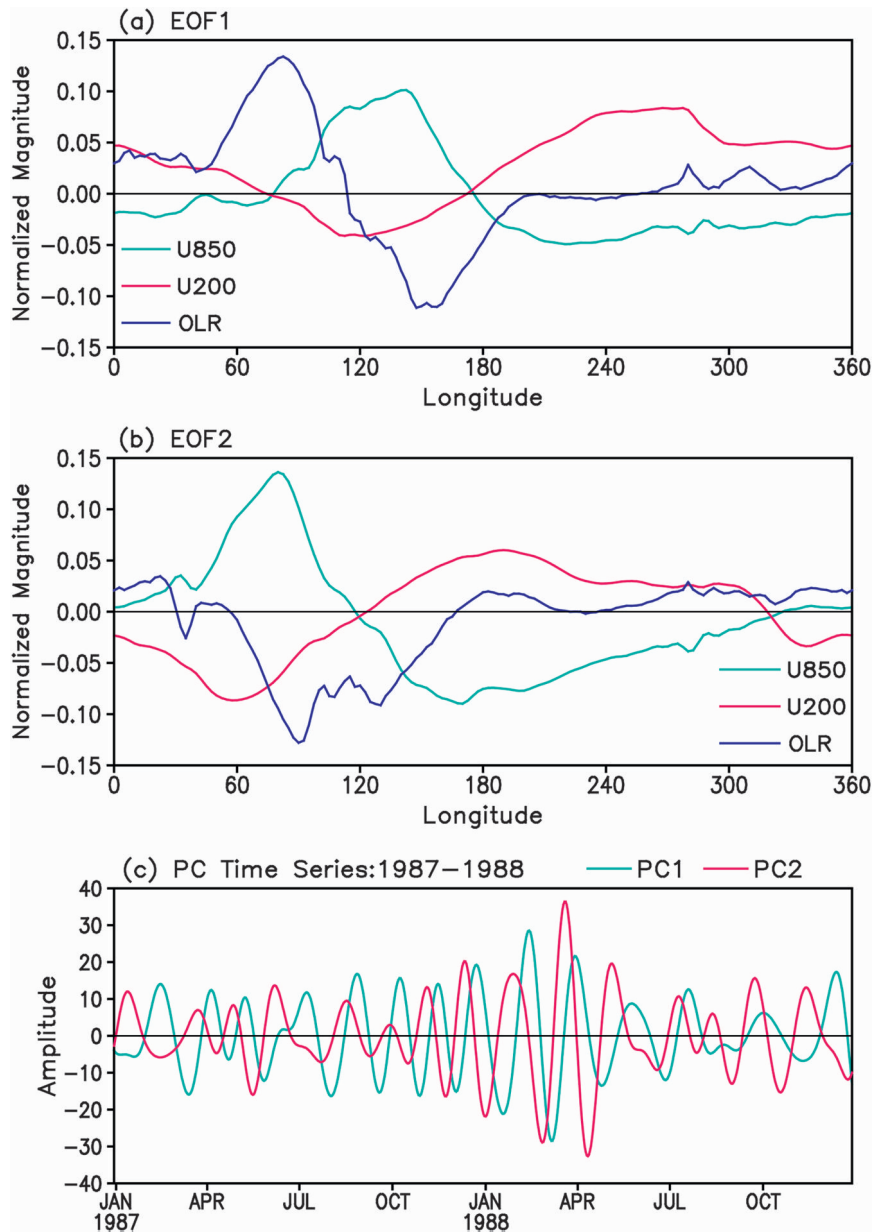


FIG. 5. EOF analysis of the combined fields of near-equatorially averaged (5°S – 5°N) OLR and 850- and 200-hPa zonal winds: (a) EOF1, (b) EOF2, and (c) PC1 and PC2 from 1 Jan 1987 to 31 Dec 1988.

quadrature to those of EOF1 (Fig. 5b). Figure 5c shows the PC time series of combined fields for 1987–88. PC2 leads PC1 by about one-quarter of a cycle, describing the eastward-propagating feature of the MJO. In a similar way, based on the NLE approach, the predictability limit of the MJO can be determined by investigating the mean error growth of \mathbf{Z} , which consists of PC1 and PC2. In Fig. 6, the predictability limit of the MJO is determined to be approximately 41 days, slightly higher than the limits shown in Figs. 2 and 4. This result in-

dicates that the coupled characteristics of large-scale convection and circulation of the MJO can enhance the predictability of the MJO to a certain extent.

According to the above analysis, the predictability of the MJO obtained by the NLE approach is more than 5 weeks for the time-filtered OLR and 850- and 200-hPa zonal winds. This result is encouraging for subseasonal forecasting, because it exceeds the performance of most numerical and statistical prediction models. However, temporal filtering is restricted for real-time prediction

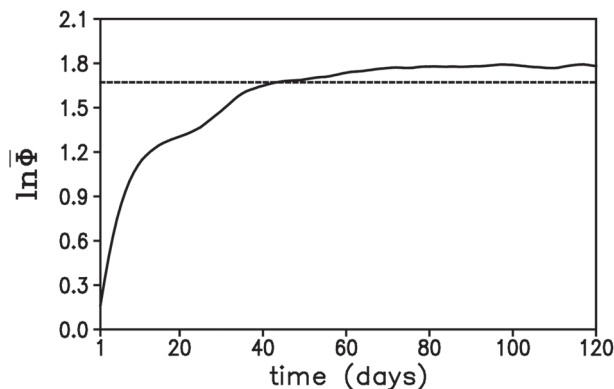


FIG. 6. As in Fig. 2, but for mean error growth of Z in the two-dimensional phase space defined by the first two PCs of EOF analysis of the combined fields of OLR and 850- and 200-hPa zonal winds (see Fig. 5).

because of its requirement for information beyond the end of the time series (Wheeler and Hendon 2004). When temporal filtering is applied, the filtered value for the present day contains information from both past and future days. Because the filtered value contains future information, it tends to inflate the forecast skill as a result of the propagation of observed information into the forecast data (Seo et al. 2009).

We apply the Monte Carlo method to test whether the enhanced predictability associated with the time-filtered data can be generated from the filtering itself or whether it arises from the underlying MJO signal within the filter band. First, we generate a set of random numbers with the same spectral characteristics as the tropical OLR data (to be specific, we take the space–time fast Fourier transform of the entire OLR dataset along the equator, multiply it by its conjugate, and then generate random complex numbers that give the same power at each wavenumber and frequency as the OLR data). Then, we compute the inverse space–time Fourier transform over the wavenumber–frequency band of the MJO to obtain the filtered noise characterized by the same spectrum as the real MJO. Last, we apply the NLE approach to a time series from the filtered noise and test its predictability. Different from the real MJO data, the evolution of the filtered noise is totally random. Therefore, when the NLE algorithm is applied to the filtered noise, the evolution information of the analogous point should not be considered. We only make the initial distance between the reference point and analogous point smallest in the NLE algorithm. The above procedure is repeated 1000 times, yielding 1000 values of the predictability limit of filtered noise. Figure 7 shows the probability distribution of these 1000 bootstrap values, which are sorted from smallest to largest (the 975th

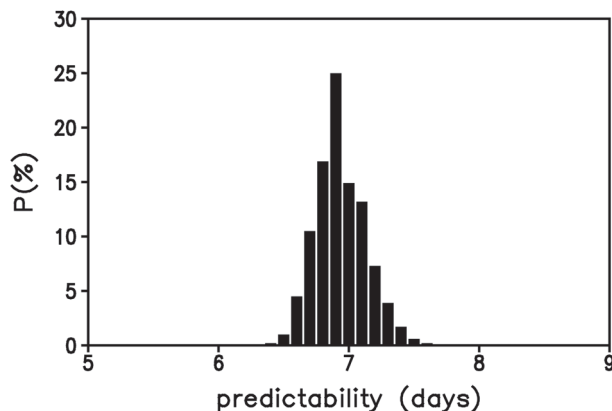


FIG. 7. Probability distribution of the predictability limit based on filtered background noise.

value is about 7 days; i.e., the threshold value of the 95% significance level). We then take a time series from the filtered OLR at a certain geographical point along the equator and test its predictability using the NLE approach. The results show that the predictability limit of the filtered OLR at almost all points along the equator is above 30 days, suggesting that the predictability of the filtered OLR is significantly greater than that of the filtered noise at the 95% level for most regions across the tropics. The predictability associated with filtered noise is artificial and arises only from the filtering itself (i.e., the noise does not contain any MJO signal). Because the filtered real data have predictability values that far exceed 7 days, we can conclude that the estimated predictability of the MJO is not from the bandpass filtering itself but from the real signal of the physical process, although the filtering tends to add up the predictability to some extent. The predictability of the MJO based on the time-filtered data can be regarded as the potential predictability of the MJO.

For the purpose of real-time monitoring and prediction of the MJO, Wheeler and Hendon (2004) recently introduced a new MJO index without time filtering. This index is based on the first two EOFs of the combined fields of near-equatorially averaged (15°S – 15°N) 850- and 200-hPa zonal winds and OLR data. The projection of daily observation data onto such multiple-variable EOFs yields PC time series that vary mainly on the intraseasonal time scale of the MJO only. The pair of PC time series that form the index are referred to as the real-time multivariate MJO series 1 (RMM1) and 2 (RMM2). Although no bandpass time filtering is applied, the index is able to strongly discriminate the 30–80-days signal. Based on this daily RMM index, the predictability of the MJO can be further explored using the NLE approach. Figure 8 shows the mean error

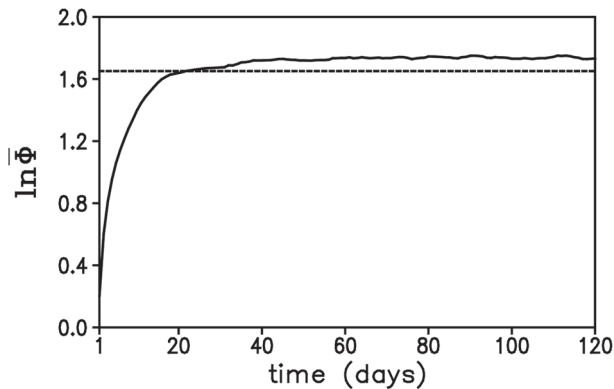


FIG. 8. As in Fig. 2, but for mean error growth of \mathbf{Z} in the two-dimensional phase space defined by the daily RMM index.

growth of \mathbf{Z} , which consists of RMM1 and RMM2, as in Eq. (1). The predictability limit of the MJO based on this daily RMM index is approximately 21 days, much lower than the potential predictability of 36–41 days obtained above. Figure 9 shows the time series of RMM1 and RMM2 for 1987 and 1988. Intraseasonal variations associated with the MJO are clearly evident in the figure, with RMM2 lagging RMM1 by 10–15 days. However, there are still day-to-day variations in the series, as noted by Wheeler and Hendon (2004). These fluctuations are systematically associated with convectively coupled Kelvin waves and equatorial Rossby waves (Roundy et al. 2009), which result in the observed day-to-day erratic variations in the RMM1 and RMM2. Given the consideration that noise (i.e., signals unrelated to the MJO) is not totally removed from the RMM index, the predictability limit in the real-time prediction of the MJO is possibly underestimated by the RMM index. The use of pentad-mean data in the real-time prediction of the MJO may be effective in removing high-frequency transients associated with weather events, thereby extending the predictability of the MJO.

In Fig. 10, the pentad-mean RMM index has a predictability limit of approximately 25–30 days, significantly longer than that obtained from the daily RMM index (Fig. 8). At present, the prediction skills of statistical models using the RMM index are generally on the order of 15–20 days of lead time (Maharaj and Wheeler 2005; Jiang et al. 2008; Seo et al. 2009), indicating that a further increase in prediction skill of the MJO may be obtainable through model improvements. Love et al. (2008) presented a different kind of real-time extraction method of the intraseasonal signal using empirical mode decomposition (EMD). The EMD technique has problems with end effects (degradation toward the end of the data record). Although some efforts have been made to minimize the end effects, they can be very large under certain circumstances (see online at http://envam1.env.uea.ac.uk/mjo_emd_archive.html), leading to a bias in estimates of MJO predictability. For real-time application, the better extraction of the intraseasonal signal remains a task in progress. Given the advantage of the RMM index in monitoring real-time MJO activity and its relative simplicity in calculation, future work should seek to reduce the influence of day-to-day variations in the RMM index on MJO predictability.

5. Summary

Based on the NLE approach recently introduced by the authors, the upper limit of the MJO predictability was investigated using the bandpass-filtered (30–80 days) OLR and 850- and 200-hPa zonal winds. Similar results were found for all of these filtered fields. The predictability limit of the MJO is about 5 weeks, far greater than that obtained by existing models and well above the 1-week predictability of background noise caused by bandpass filtering. This result is encouraging for subseasonal forecasting; however, time filtering contains future information, thereby possibly overestimating the predictability of the MJO. For real-time

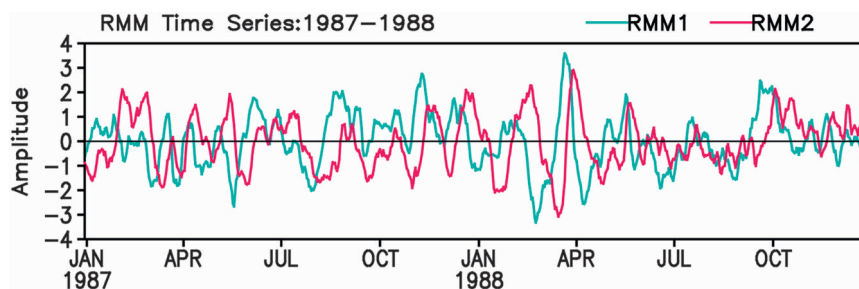


FIG. 9. Real-time multivariate MJO series 1 (RMM1) and 2 (RMM2) from 1 Jan 1987 to 31 Dec 1988, as introduced by Wheeler and Hendon (2004).

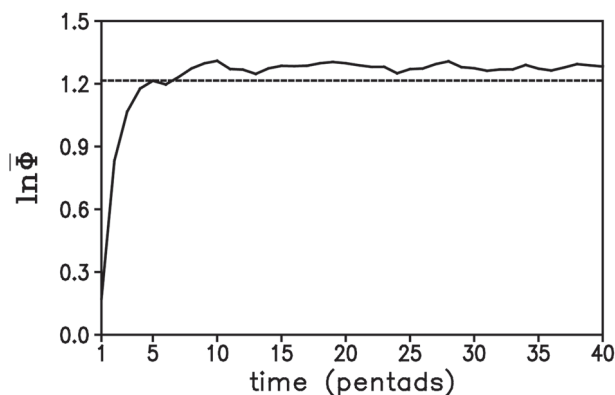


FIG. 10. As in Fig. 8, but for mean error growth of Z in the two-dimensional phase space defined by the pentad-mean RMM index.

prediction of the MJO, time filtering is restricted and the predictability of the MJO could be lower than the above estimate. An investigation of the predictability of the real-time MJO index introduced by Wheeler and Hendon (2004) raises the possibility that the upper limit of the forecast skill in the real-time prediction of the MJO can exceed 3 weeks. These results represent a wide range of estimates of MJO predictability rather than an estimate presented as a specific number of days. Figure 11 summarizes the range of MJO predictabilities estimated in this paper. The useful predictive skill of the MJO can exist out to at least 3 weeks and possibly longer (out to 5 weeks). The differences between the real-time predictability and potential predictability of the MJO depend on the intraseasonal signals obtained using various extraction methods. Given the future developments of extraction methods for the intraseasonal signal, it is likely that the range of estimates of MJO predictability will be reduced in the future.

Because observation data contain components of both atmospheric internal dynamics and external forcings from the ocean, it is difficult to separate their individual contributions to MJO predictability. The roles of initial conditions and external forcings in the MJO predictability remain to be studied in the future using a more realistic model of the MJO. The MJO predictability obtained in this study only provides an estimate of the average predictability of the MJO. For strong and weak MJO events, the predictability may be different from that estimated. The predictability of the MJO is also dependent on its phase (Waliser et al. 2003; Fu et al. 2007). These points will require further study using the NLE approach. Another important point to be considered is seasonal variations in intraseasonal oscillation. Tropical intraseasonal variability shows two dominant modes: the boreal winter Madden-Julian

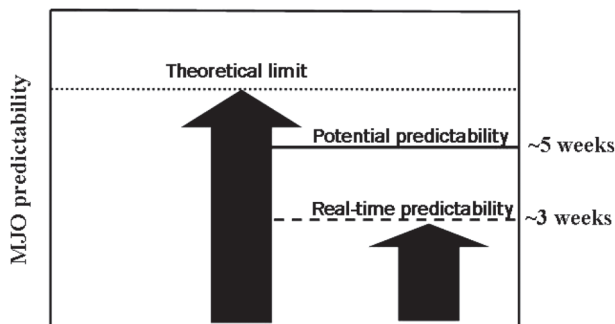


FIG. 11. Simplified diagram showing the range of estimates of MJO predictability obtained in this paper.

oscillation (MJO) and the boreal summer intraseasonal oscillation (ISO). The MJO is characterized by eastward-propagating tropical convective anomalies and associated circulation anomalies. In contrast, the ISO has a complex structure that exhibits both eastward and northward propagation (Yasunari 1979; Lawrence and Webster 2002). Given that the EOFs of the year-round daily data tend to be dominated by the stronger boreal winter phase (MJO) of intraseasonal variability, this study mainly considers boreal winter MJO cases. Further study is necessary to assess differences in the predictability of boreal summer ISO and boreal winter MJO.

Acknowledgments. We thank three anonymous reviewers for helpful comments and suggestions and Dr. Jiangyu Mao and Dr. Zhiwei Wu for useful advice and comments. In particular, the predictability calculation for filtered random background noise suggested by one reviewer greatly improved the interpretation of the results. Funding for this research was provided jointly by NSFC Projects (40805022 and 40675046) and the 973 program (2006CB403600). Author Seo was funded by the Korea Meteorological Administration Research and Development Program under Grant CATER 2007-4208.

REFERENCES

- Ding, R. Q., and J. P. Li, 2007: Nonlinear finite-time Lyapunov exponent and predictability. *Phys. Lett.*, **364A**, 396–400.
- , —, and K. J. Ha, 2008: Trends and interdecadal changes of weather predictability during 1950s–1990s. *J. Geophys. Res.*, **113**, D24112, doi:10.1029/2008JD010404.
- Ferranti, L., T. N. Palmer, F. Molteni, and K. Klinker, 1990: Tropical-extratropical interaction associated with the 30–60 day oscillation and its impact on medium and extended range prediction. *J. Atmos. Sci.*, **47**, 2177–2199.
- Fu, X., B. Wang, D. Waliser, and L. Tao, 2007: Impact of atmosphere–ocean coupling on the predictability of monsoon intraseasonal oscillations. *J. Atmos. Sci.*, **64**, 157–174.
- Goswami, B. N., and P. K. Xavier, 2003: Potential predictability and extended range prediction of Indian summer

- monsoon breaks. *Geophys. Res. Lett.*, **30**, 1966, doi:10.1029/2003GL017810.
- Hartmann, D. L., M. L. Michelsen, and S. A. Klein, 1992: Seasonal variations of tropical intraseasonal oscillations: A 20–25-day oscillation in the western Pacific. *J. Atmos. Sci.*, **49**, 1277–1289.
- Higgins, R. W., and K. C. Mo, 1997: Persistent North Pacific circulation anomalies and the tropical intraseasonal oscillation. *J. Climate*, **10**, 223–244.
- Jiang, X. N., D. E. Waliser, M. C. Wheeler, C. Jones, M.-I. Lee, and S. D. Schubert, 2008: Assessing the skill of an all-season statistical forecast model for the Madden–Julian oscillation. *Mon. Wea. Rev.*, **136**, 1940–1956.
- Jones, C., D. E. Waliser, K. M. Lau, and W. Stern, 2004: The Madden–Julian oscillation and its impact on Northern Hemisphere weather predictability. *Mon. Wea. Rev.*, **132**, 1462–1471.
- Kalnay, E., and Coauthors, 1996: The NCEP/NCAR 40-Year Reanalysis Project. *Bull. Amer. Meteor. Soc.*, **77**, 437–471.
- Kim, H.-M., C. D. Hoyos, P. J. Webster, and I.-S. Kang, 2008: Sensitivity of MJO simulation and predictability to sea surface temperature variability. *J. Climate*, **21**, 5304–5317.
- Lau, K. M., and P. H. Chan, 1986: Aspects of the 40–50-day oscillation during the northern summer as inferred from outgoing longwave radiation. *Mon. Wea. Rev.*, **114**, 1354–1367.
- Lawrence, D. M., and P. J. Webster, 2002: The boreal summer intraseasonal oscillation: Relationship between northward and eastward movement of convection. *J. Atmos. Sci.*, **59**, 1593–1606.
- Li, J. P., and R. Q. Ding, 2008: Temporal-spatial distributions of predictability limit of short-term climate (in Chinese with English abstract). *Chin. J. Atmos. Sci.*, **32**, 975–986.
- , —, and B. H. Chen, 2006: Review and prospect on the predictability study of the atmosphere. *Review and Prospects of the Developments of Atmosphere Sciences in Early 21st Century*, China Meteorology Press, 96–104.
- Liebmann, B., and C. A. Smith, 1996: Description of a complete (interpolated) outgoing longwave radiation dataset. *Bull. Amer. Meteor. Soc.*, **77**, 1275–1277.
- , H. H. Hendon, and J. D. Glick, 1994: The relationship between tropical cyclones of the western Pacific and Indian Oceans and the Madden–Julian oscillation. *J. Meteor. Soc. Japan*, **72**, 401–411.
- Lorenz, E. N., 1965: A study of the predictability of a 28-variable atmospheric model. *Tellus*, **17**, 321–333.
- , 1982: Atmospheric predictability experiments with a large numerical model. *Tellus*, **34**, 505–513.
- Love, B. S., A. J. Matthews, and G. J. Janacek, 2008: Real-time extraction of the Madden–Julian oscillation using empirical mode. *J. Climate*, **21**, 5318–5335.
- Madden, R. A., and P. R. Julian, 1994: Observations of the 40–50-day tropical oscillation—A review. *Mon. Wea. Rev.*, **122**, 814–837.
- Maharaj, E. A., and M. C. Wheeler, 2005: Forecasting an index of the Madden-oscillation. *Int. J. Climatol.*, **25**, 1611–1618.
- Maloney, E. D., and D. L. Hartmann, 1998: Frictional moisture convergence in a composite life cycle of the Madden–Julian Oscillation. *J. Climate*, **11**, 2387–2403.
- Matthews, A. J., 2000: Propagation mechanisms for the Madden–Julian oscillation. *Quart. J. Roy. Meteor. Soc.*, **126**, 2637–2652.
- Nakazawa, T., 1986: Intraseasonal variations of OLR in the Tropics during the FGGE year. *J. Meteor. Soc. Japan*, **64**, 17–34.
- North, G. R., T. L. Bell, R. F. Cahalan, and F. J. Moeng, 1982: Sampling errors in the estimation of empirical orthogonal function. *Mon. Wea. Rev.*, **110**, 699–706.
- Reichler, T., and J. O. Roads, 2005: Long-range predictability in the tropics. Part II: 30–60-day variability. *J. Climate*, **18**, 634–650.
- Roundy, P. E., C. J. Schreck III, and M. A. Janiga, 2009: Contributions of convectively coupled equatorial Rossby waves and Kelvin waves to the real-time multivariate MJO indices. *Mon. Wea. Rev.*, **137**, 363–372.
- Seo, K.-H., J.-K. E. Schemm, C. Jones, and S. Moorthi, 2005: Forecast skill of the tropical intraseasonal oscillation in the NCEP GFS dynamical extended range forecasts. *Climate Dyn.*, **25**, 265–284.
- , —, W. Wang, and A. Kumar, 2007: The boreal summer intraseasonal oscillation simulated in the NCEP Climate Forecast System (CFS): The effect of sea surface temperature. *Mon. Wea. Rev.*, **135**, 1807–1827.
- , W. Wang, J. Gottschalck, Q. Zhang, J. K. E. Schemm, W. R. Higgins, and A. Kumar, 2009: Evaluation of MJO forecast skill from several statistical and dynamical forecast models. *J. Climate*, **22**, 2372–2388.
- Van den Dool, H. M., and S. Saha, 1990: Frequency dependence in forecast skill. *Mon. Wea. Rev.*, **118**, 128–137.
- Waliser, D. E., N. E. Graham, and C. Gautier, 1993: Comparison of highly reflective cloud and outgoing longwave radiation datasets for use in estimating tropical convection. *J. Climate*, **6**, 331–353.
- , K. M. Stern, and C. Jones, 2003: Potential predictability of the Madden–Julian oscillation. *Bull. Amer. Meteor. Soc.*, **84**, 33–50.
- Wang, B., and H. Rui, 1990: Synoptic climatology of transient tropical intraseasonal convection anomalies: 1975–1985. *Meteor. Atmos. Phys.*, **44**, 43–61.
- Wheeler, M., and H. H. Hendon, 2004: An all-season real-time multivariate MJO index: Development of an index for monitoring and prediction. *Mon. Wea. Rev.*, **132**, 1917–1932.
- Yasunari, T., 1979: Cloudiness fluctuation associated with the Northern Hemisphere summer monsoon. *J. Meteor. Soc. Japan*, **57**, 227–242.
- , 1980: A quasi-stationary appearance of the 30–40 day period in the cloudiness fluctuations during the summer monsoon over India. *J. Meteor. Soc. Japan*, **58**, 336–354.